Astronomy & Astrophysics

The OTELO survey

A case study of [O III] λ4959,5007 emitters at $\langle z \rangle = 0.83$

Ángel Bongiovanni[1,2,3,4], Marina Ramón-Pérez[2,3], Ana María Pérez García[5,4], Miguel Cerviño[5,2,7], Jordi Cepa[2,3,4], Jakub Nadolny[2,3], Ricardo Pérez Martínez[6,4], Emilio J. Alfaro[7], Héctor O. Castañeda[13], Bernabé Cedrés[2,3], José A. de Diego[12], Alessandro Ederoclite[11,4], Mirian Fernández-Lorenzo[7], Jesús Gallego[9], José de Jesús González[12], José Ignacio González-Serrano[8,4], Maritza A. Lara-López[18], Iván Oteo Gómez[16,17], Carmen P. Padilla Torres[21], Irene Pintos-Castro[15], Mirjana Pović[14,7], Miguel Sánchez-Portal[1,4], D. Heath Jones[19], Joss Bland-Hawthorn[20], and Antonio Cabrera-Lavers[10]

[1] Instituto de Radioastronomía Milimétrica (IRAM), Av. Divina Pastora 7, Núcleo Central 18012, Granada, Spain
e-mail: bongio@iram.es
[2] Instituto de Astrofísica de Canarias (IAC), 38200 La Laguna, Tenerife, Spain
[3] Departamento de Astrofísica, Universidad de La Laguna (ULL), 38205 La Laguna, Tenerife, Spain
[4] Asociación Astrofísica para la Promoción de la Investigación, Instrumentación y su Desarrollo, ASPID, 38205 La Laguna, Tenerife, Spain
[5] Centro de Astrobiología (CSIC/INTA), 28692 ESAC Campus, Villanueva de la Cañada, Madrid, Spain
[6] ISDEFE for European Space Astronomy Centre (ESAC)/ESA, PO Box 78, 28690 Villanueva de la Cañada, Madrid, Spain
[7] Instituto de Astrofísica de Andalucía, CSIC, 18080 Granada, Spain
[8] Instituto de Física de Cantabria (CSIC-Universidad de Cantabria), 39005 Santander, Spain
[9] Departamento de Física de la Tierra y Astrofísica, Instituto de Física de Partículas y del Cosmos, IPARCOS, Universidad Complutense de Madrid, 28040 Madrid, Spain
[10] Grantecan S. A., Centro de Astrofísica de La Palma, Cuesta de San José, 38712 Breña Baja, La Palma, Spain
[11] Universidade de São Paulo, Instituto de Astronomia, Geofísica e Ciências Atmosféricas, 05508090 São Paulo, SP, Brazil
[12] Instituto de Astronomía, Universidad Nacional Autónoma de México, 04510 Ciudad de México, Mexico
[13] Departamento de Física, Escuela Superior de Física y Matemáticas, Instituto Politécnico Nacional, 07738 Ciudad de México, Mexico
[14] Ethiopian Space Science and Technology Institute (ESSTI), Entoto Observatory and Research Center (EORC), Astronomy and Astrophysics Research Division, PO Box 33679, Addis Ababa, Ethiopia
[15] Department of Astronomy & Astrophysics, University of Toronto, Toronto, Canada
[16] Institute for Astronomy, University of Edinburgh, Royal Observatory, Blackford Hill, Edinburgh EH9 3HJ, UK
[17] European Southern Observatory, Karl-Schwarzschild-Str. 2, 85748 Garching, Germany
[18] DARK, Niels Bohr Institute, University of Copenhagen, Lyngbyvej 2, Copenhagen 2100, Denmark
[19] English Language and Foundation Studies Centre, University of Newcastle, Callaghan, NSW 2308, Australia
[20] Sydney Institute of Astronomy, School of Physics, University of Sydney, Sydney, NSW 2006, Australia
[21] INAF, Telescopio Nazionale Galileo, Apartado de Correos 565, 38700 Santa Cruz de la Palma, Spain

ABSTRACT

Context. The OSIRIS Tunable Filter Emission Line Object (OTELO) survey is a very deep, blind exploration of a selected region of the Extended Groth Strip and is designed for finding emission-line sources (ELSs). The survey design, observations, data reduction, astrometry, and photometry, as well as the correlation with ancillary data used to obtain a final catalogue, including photo-z estimates and a preliminary selection of ELS, were described in a previous contribution.

Aims. Here, we aim to determine the main properties and luminosity function (LF) of the [O III] ELS sample of OTELO as a scientific demonstration of its capabilities, advantages, and complementarity with respect to other surveys.

Methods. The selection and analysis procedures of ELS candidates obtained using tunable filter pseudo-spectra are described. We performed simulations in the parameter space of the survey to obtain emission-line detection probabilities. Relevant characteristics of [O III] emitters and the LF ([O III]), including the main selection biases and uncertainties, are presented.

Results. From 541 preliminary emission-line source candidates selected around $z = 0.8$, a total of 184 sources were confirmed as [O III] emitters. Consistent with simulations, the minimum detectable line flux and equivalent width in this ELS sample are $\sim 5 \times 10^{-19}$ erg s^{-1} cm^2 and ~ 6 Å, respectively. We are able to constrain the faint-end slope ($\alpha = -1.03 \pm 0.08$) of the observed LF ([O III]) at a mean redshift of $z = 0.83$. This LF reaches values that are approximately ten times lower than those from other surveys. The vast majority (84%) of the morphologically classified [O III] ELSs are disc-like sources, and 87% of this sample is comprised of galaxies with stellar masses of $M_\star < 10^{10}\,M_\odot$.

Key words. techniques: imaging spectroscopy – surveys – catalogs – galaxies: starburst – galaxies: active – galaxies: luminosity function, mass function

1. Introduction

The analysis of the strength and profile of emission lines in galaxy spectra provides basic information about the kinematics, density temperature, and chemical composition of the ionised gas, allowing inferences about dust extinction, star-formation rate, and gas outflows. This enables spectral classification diagnostics between pure star-forming galaxies (SFGs) and hosts of active galactic nuclei (AGNs) independently of the galaxy mass. As such, the detection and characterisation of sources with strong nebular emission lines (emission-line sources or ELSs) can provide a wealth of information about galaxy populations and the mechanisms that shape the galaxy-evolution process.

Dwarf galaxies are not only more numerous than other types of galaxies with intermediate and high masses, but also constitute the building blocks of the more massive galaxies within the framework of the hierarchical model of galaxy evolution (White & Frenk 1991; Somerville & Primack 1999; Benson et al. 2003; Somerville et al. 2012), which would imply an increased number of them with redshift. However, little is known about their nature, growth, evolution, or star formation modes; this is particularly true for low- and very-low-mass galaxies, that is, those with $\log(M_\star[M_\odot]) \approx 7-9$ (De Lucia et al. 2014). Knowledge of the real contribution of dwarf galaxies to the luminosity function (LF) at any epoch is essential for understanding various aspects of galaxy evolution (Klypin et al. 2015), from reionisation phenomena to the fossil records in the Local Group. Deep extragalactic surveys for finding faint ELSs, and model-based synthetic galaxy catalogues -with their synergies- are fundamental tools in tackling this problem.

From the first photographic atlases (e.g. those of Sandage 1961; Arp 1966) to the most recent and ongoing surveys, such as SDSS (Strauss et al. 2002), VVDS-CFDS (Le Fèvre et al. 2004), zCOSMOS (Lilly et al. 2007), GAMA (Driver et al. 2009) DEEP2 (Newman et al. 2013), eBOSS (Dawson et al. 2016), DES (Dark Energy Survey Collaboration 2016), DEVILS (Davies et al. 2018), hCOSMOS (Damjanov et al. 2018), VANDELS (McLure et al. 2018), and VIPERS (Scodeggio et al. 2018), the number and variety of extragalactic explorations have resulted in a growing understanding of the key connections between physical processes and fundamental galaxy observables. In view of this, realistic model-based mock catalogues of galaxies are needed to isolate the net effects and uncertainties of determined physical galaxy properties on observed galaxies, depending on the techniques used to gather real galaxy data. Narrow-band (NB) and intermediate-band (IB) imaging stand out among these techniques for finding ELSs because they do not suffer from the selection biases and can go deeper in flux than classical spectroscopy. Surveys such as COMBO-17 (Wolf et al. 2003), ALHAMBRA (Moles et al. 2008), SHARDS (Pérez-González et al. 2013), J-PAS (Benitez et al. 2014), CF-HiZELS (Sobral et al. 2015), and the Hyper Suprime-Cam Subaru Strategic Program (HSC-SSP; Hayashi et al. 2018, and references therein) have used this approach to isolate significantly large samples of ELSs in surveys of differently sized comoving volumes.

Even though the NB deep-imaging technique with wide fields of view has been shown to be effective for this purpose, in contrast to the conventional spectroscopic surveys because of their proper selection biases and required observing time, its sensitivity to low values of equivalent width (EW) is set by the passband of the filter used. The line EW of most very faint ELSs is too small to allow isolation of ELS candidates in classical NB surveys or their continua is too faint to allow them to be selected as science targets in current spectroscopic

surveys. A compromise solution is the NB scan technique. The OSIRIS Tunable Filter Emission Line Object (OTELO) survey combines the advantages of blind, deep NB surveys with the typical EW sensitivity of the spectroscopic approach for finding dwarf galaxies at low and intermediate redshifts, with a similar performance as that provided by integrated light surveys for detecting these galaxies in the Local Volume (Danieli et al. 2018). In any case, it is foreseeable that future projects such as LSST (LSST Science Collaboration 2009) on very deep NB explorations (Yoachim et al. 2019) and spectroscopic surveys such as Euclid (Laureijs et al. 2011), WFIRST (Dressler et al. 2012), and WAVES (Driver et al. 2016) will allow very faint ELS candidates to be detected in great numbers and completeness.

The aim of this study is to test the potential of OTELO for finding dwarf SFGs through the analysis of an [O III] ELS sample at intermediate redshift in order to constrain its number density by probing the faint end of the LF([O III]), and prepare the way for studying their intrinsic properties.

The [O III] line originates from the gas that is highly ionised by photons from young massive stars in the HII regions of galaxies, but is also linked to the narrow-line region (NLR) of AGNs similarly to other strong forbidden lines seen in the spectra of low-density plasmas (Stasińska 2007). Although biased towards low gas metallicity in high-ionisation conditions, which also generally imply low stellar masses (Suzuki et al. 2016, and references therein), this emission line can therefore be used as a tracer of star formation. Furthermore, the prominence of [O III] emission among the strongest lines in the optical spectra of these types of sources, as well as its easily recognisable doublet, makes this emission line the first choice to examine the performance of any tunable filter survey dedicated to the search for ELSs.

On the other hand, the observed number density of low-mass ELSs, which have shallow gravitational potential wells, is affected by the dominant physical processes that regulate star formation triggering or quenching in such galaxies (Brough et al. 2011). The faint end slope of the LF in SFGs -as a way to express that number statistic- and its evolution remain as unresolved issues because most recent studies suffer from significant incompleteness at luminosities of $\log(L[L_\odot]) \lesssim 8-9$ and star formation rates (SFRs) lower than 0.1 $M_\odot$ yr^{-1} (Bothwell et al. 2011). Evidently, these problems can be progressively solved by unbiased, very deep small-area surveys (Parsa et al. 2016).

This paper is structured as follows. In Sect. 2, we describe the OTELO survey and its main products. Section 3 outlines the general ELS selection and analysis procedures from OTELO data. In Sect. 4 we estimate the main characteristic parameters of the survey as a function of the probability of emission-line detection based on educated simulations of OTELO products. Section 5 is devoted to obtaining and characterising the final [O III] ELS sample at a mean redshift of $\langle z \rangle = 0.83$ according to the general procedure. In Sect. 6, an observed LF is given after summarising the main survey biases and uncertainties that affect it. The analysis of this LF and a comparison with similar data reported in the recent literature are given in Sect. 7. The last section contains a compendium of the work presented.

For consistency with recent contributions related to the main subject of this paper, we assume a standard Λ-CDM cosmology with $\Omega_\Lambda = 0.7$, $\Omega_m = 0.3$, and $H_0 = 70$ km s^{-1} Mpc^{-1}. All magnitudes are given in the AB system.

2. The OTELO survey data

The OTELO survey is an NB imaging survey that scans a spectral window of about 230 Å centred at ~9175 Å. This window

is substantially free from strong airglow emission. The survey uses the red tunable filter (RTF) of the OSIRIS instrument on the 10.4 m Gran Telescopio Canarias (GTC, Álvarez et al. 1998) to produce spectral tomography (resolution $R \sim 700$) composed of 36 slices, each of 12 Å in full width at half maximum (FWHM) and tuned between 9070 and 9280 Å every 6 Å. The net integration time for each slice was 6.6 ks. The spectral sampling adopted is a compromise between an intended photometric accuracy of ~20% in the deblending of the Hα and [N II] $\lambda6548,6583$ emission lines observed at $z \sim 0.4$ and a reasonably short observing time frame.

The OTELO field is located in a selected region of ~56 arcmin^2 in the Extended Groth Strip (EGS). This region is embedded in Deep Field 3 of the Canada–France–Hawaii Telescope Legacy Survey[1] (CFHTLS), which forms part of the collaborative All-Wavelength EGS International Survey (AEGIS, Davis et al. 2007). The design of the OTELO RTF scan aims to perform a blind search of mainly extragalactic sources in as many disjoint cosmological volumes between redshift $z = 0.4$ and ~6.5 as possible in which strong emission lines can be observed in the wavelength range explored. The characteristics and data products of OTELO, and the general demographics of the detected targets are given in the survey presentation paper (Bongiovanni et al. 2019, hereafter referred to as OTELO-I). Likewise, that paper contains a full description of the tunable filters (TFs), particularly the properties of the RTF.

The coaddition of the 36 NB slices of OTELO was used both for a blind source detection in a custom deep image (OTELO-Deep) to create an IB magnitude (OTELO$_{Int}$, 230 Å wide) and to measure the fluxes of those sources detected in registered and resampled images in the optical u, g, r, i, and z bands from CFHTLS (T0007 Release), and in the J, H, and K_s bands of the near-infrared (NIR) from the WIRcam Deep Survey (WIRDS, Bielby et al. 2012, Release T0002). The resulting catalogue containing 11 237 entries was carefully cross-matched with ancillary X-ray through far-infrared (FIR) data, including GALEX FUV/NUV[2] data from the four channels of *Spitzer*/IRAC, FIR data from *Spitzer*/MIPS at 24 μm, and from PEP/*Herschel* (Lutz et al. 2011) at 100 and 160 μm. Finally, photometric redshift (photo-z or z_{phot}) and extinction estimates obtained from all these data using the LePhare code (Arnouts et al. 1999; Ilbert et al. 2006), as well as redshift data from other surveys (DEEP2 and CFHTLS), were included in the dubbed OTELO multi-wavelength catalogue. Further details about this catalogue and other survey products are described in OTELO-I. For a quick reference, the main features of the survey and its catalogue are summarised in Table 1.

Each source in the catalogue of OTELO is paired with exactly one pseudo-spectrum, which is defined as a vector composed of a succession of error-weighted averages of the fluxes measured on the individual RTF images at the same wavelength in the tomography described above. Hence, a pseudo-spectrum of OTELO is formed by a set of at least 36 flux elements evenly spaced by 6 Å. Unlike spectra obtained by diffraction devices, a pseudo-spectrum is the result of the convolution in the wavelength space of the input spectral energy distribution (SED) of a given source, with the RTF instrumental response characterised by a succession of Airy profiles. The wavelength sampling of OTELO pseudo-spectra is about one-third of the effective passband $\delta\lambda_e$ of an RTF slice (see Table 1). Consequently, line

Table 1. Main features of the OTELO survey and its multi-wavelength catalogue.

| Parameter	Value
Field coordinates (RA, Dec)	14 17 33, +52 28 22
Effective surveyed area	$7.5' \times 7.4'$
Wavelength range of RTF tunings	9070–9280 Å
RTF slice width ($\delta\lambda_{FWHM}$)	12 Å
RTF sampling interval	$\delta\lambda_{FWHM}/2 = 6$ Å
RTF slice effective passband ($\delta\lambda_e$)	$\frac{\pi}{2}\delta\lambda_{FWHM} \simeq 19.4$ Å
Wavelength accuracy	1 Å
Number of RTF tunings	36
Spectral range of pseudo-spectra	230 Å
Total integration time per slice	6×1100 s
Mean PSF in RTF images	$0.87 \pm 0.13''$
m_{lim} –OTELO$_{Int}$ (3σ; 50% compl.)	26.38 mag
Mean error at m_{lim}	0.33 mag
Total entries in the catalogue	11 237
Number of ancillary data bands	18
Photo-z (z_{phot}) accuracy	$\leq 0.2 (1 + z_{phot})$
Astrometric accuracy (RTF images)	$0.23''$
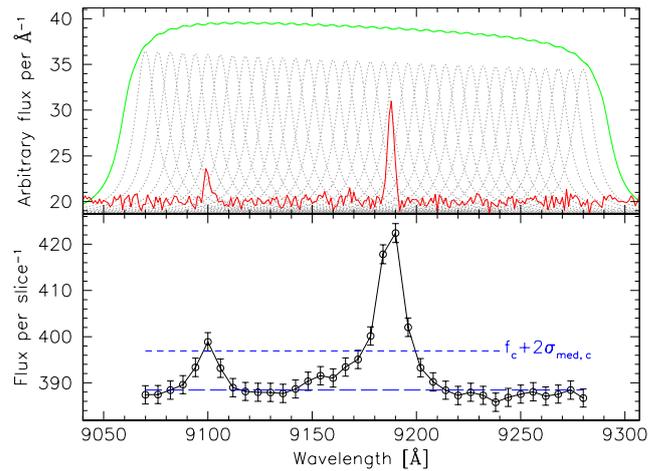
Fig. 1. Example of a synthetic pseudo-spectrum of an [O III] $\lambda4959,5007$ source as seen by OTELO. *Upper panel*: synthetic spectrum (in red) with arbitrary flux density consisting of a flat continuum plus two emission lines with Gaussian profiles ($FWHM = 2$ Å) modelling the [O III] doublet at $z = 0.835$, with Poissonian noise added. The grey dotted curves represent the Airy instrumental profiles of the OTELO RTF scan. These individual profiles can be synthesised into a custom filter response (green curve), which is useful to obtain an integrated IB flux. *Lower panel*: pseudo-spectrum obtained from the convolution of the synthetic spectrum in the upper panel with these Airy profiles, mimicking the OTELO data. The blue short-dashed line represents the $2\sigma_{med,c}$ level above the median flux or pseudo-continuum (blue long-dashed line) defined in the main text. Flux density between both spectra differs by a factor equal to the effective passband $\delta\lambda_e$ of an RTF slice.

profiles in the pseudo-spectra are particularly affected by these instrumental effects and their flux values are more correlated in the wavelength space than standard spectra. In Sect. 3.3 we describe the methodology used to correct the pseudo-spectra for these effects. Figure 1 shows an example of a synthetic pseudo-spectrum with emission lines, as seen by OTELO at the optical centre of the RTF (see Sect. 2.1 in OTELO-I).

3. Selection and analysis of emission line sources

For the purposes of this paper, the following sections detail the steps required for selection and analysis of OTELO ELSs for any cosmic volume, based on the data products described above.

3.1. Preliminary selection of emission-line sources in OTELO

A given source in the OTELO multi-wavelength catalogue qualifies as a preliminary ELS candidate if (i) at least one point of the pseudo-spectrum lies above a value defined by $f_c + 2\sigma_{\mathrm{med,c}}$, where f_c is the flux of the pseudo-continuum, which itself is defined as the median flux of the pseudo-spectra, and $\sigma_{\mathrm{med,c}}$ is the root of the averaged square deviation of the entire pseudo-spectrum with respect to f_c; and (ii) there is an adjacent point with a flux density above $f_c + \sigma_{\mathrm{med,c}}$.

Using these criteria, we found that from a blind flux excess analysis of the pseudo-spectra a subset of 6649 candidates match these conditions. This set contains all sources flagged as `els_preliminary` in the OTELO multi-wavelength catalogue. The selection criteria given above set a limit on the performance of the algorithms used for retrieving line fluxes, whether via inverse deconvolution (see Sect. 3.2) or automatic profile fitting in pseudo-spectra as done by Sánchez-Portal et al. (2015). Using a broad set of simulated OTELO pseudo-spectra such as those described in Sect. 4, we verified that if the intensity of the emission feature in the pseudo-spectra is below the thresholds indicated above, then none of these algorithms yield a plausible result.

However, there is a fraction of real ELSs whose emission line is truncated by the limits of the OTELO spectral range but that do not meet the criteria cited above. According to the RTF sampling and the wavelength range of the OTELO tomography, this fraction is about 5% if the chance of the emission-line defined above is uniformly distributed within the spectral range. These sources (as illustrated in Fig. A.1), can also be retrieved using a (z-OTELO$_{\mathrm{Int}}$) colour–magnitude diagram, where OTELO$_{\mathrm{Int}}$ is the integrated magnitude of a given source detected in the OTELO-Deep image (see Sect. 2), as long as the contrast of the emission line above the pseudo-continuum is large enough to give a reliable colour excess (see Pascual et al. 2007).

3.2. Selecting emission line sources according to the emission line

As a consequence of the characteristic phase effect of the RTF, the passband of a given OTELO pseudo-spectrum is blueshifted (and slightly narrowed) as the corresponding source is further away from the optical centre (see Eqs. (7) and (8) in OTELO-I). Accordingly, the wavelength of the peak flux λ_{peak} of an emission line in any OTELO pseudo-spectrum, independently of the mean distance of the source from the optical centre, can be found between 9280 and 8985 Å. The first of these latter two values is the reddest tuned wavelength of the OTELO scan and the second is the phase-corrected wavelength corresponding to the bluest tuning at $r_{\mathrm{max}} = 4.2$ arcminutes from the optical centre, where r_{max} is the maximum angular distance from the optical centre at which a source could be found in the OTELO field. Therefore, depending on the rest-frame wavelength of the emission line of interest, the wavelength range thus-defined allows us to determine the redshift window in which all the corresponding ELSs would fall.

Reliable redshift estimates are important for tagging the emission line(s) observed in OTELO pseudo-spectra, as is the case in any narrow band survey for the search of ELSs. The redshift of a source whose emission line falls inside the wavelength range defined above is a priori unknown. This can be solved using photo-z estimations, which nevertheless entails uncertainties. However, the by-products of these estimations also provide clues about the spectral classification of the sources to be studied.

The multi-wavelength catalogue of OTELO provides, among others, photo-z estimations obtained by a χ^2–SED fitting of the broad band ancillary data cited in Sect. 2, both including and excluding the OTELO-Deep photometry. In both cases, the z_{phot} uncertainty of each object was defined by $\delta(z_{\mathrm{phot}}) = |z_{\mathrm{phot}}(\mathrm{max}) - z_{\mathrm{phot}}(\mathrm{min})|/2$, where the maximum and minimum values of z_{phot} correspond to the limits of a 68% confidence interval of the z_{phot} probability distribution function (PDF).

For selecting ELSs it is wise to employ the photo-z solutions that include the OTELO-Deep photometry (labeled `z_BEST_deepY` in the catalogue) and its uncertainties. The overall accuracy of these photo-z estimations is better than $0.2(1 + z_{\mathrm{phot}})$ – see Table 1 – and the 1σ width for $z_{\mathrm{phot}} \lesssim 1.5$ is around 0.06. The redshift window defined above should be slightly broadened according to this width. All the sources with a photo-z value within the resulting redshift window, and that meet the condition given by $\delta(z_{\mathrm{phot}}) \leq 0.2(1 + z_{\mathrm{phot}})$, then pass to the next analysis stage.

It should be mentioned that the observed SED of a small but noticeable fraction of ELSs could be better fitted with AGN templates, as expected. The necessary data to compare the goodness-of-fit of the photo-z depending on the template used are also given in the multiwavelength catalogue. For these cases, using a z_{phot} obtained from the templates labeled `AGN/QSOs` in OTELO-I can help to complete the source selection according to the scientific goals pursued.

Once the pseudo-spectra of the preliminary ELS candidates in the corresponding photo-z range have been identified, they must be further examined in order to (i) discard artefacts or spurious sources (i.e. multiple peaks in pseudo-spectra linked to correlated sky noise, badly deblended sources in the OTELO-Deep image, objects near the boundary of the gap between detectors creating false features in pseudo-spectra, and residuals of diffraction spikes from bright sources), and interlopers with real emission lines (see Sect. 3.3); (ii) flag other interesting spectral features or anomalies (i.e. line truncation or possible absorption lines); and (iii) assign a redshift value to the peak of the observed features in the pseudo-spectrum, or "guess" this value. The wavelength accuracy of this procedure is ±3 Å, which translates to a redshift accuracy of about $10^{-3}(1 + z)$, which itself is refined using the inverse deconvolution algorithm described in Sect. 3.3.

A web-based graphic user interface (GUI) facility, which was prepared for the public release of OTELO data, can be used to carry out these tasks. This tool presents a complete dossier of every source in the survey, including observed SEDs, best-template fittings, broad-band image cutouts, cross-references with other public databases, and the pseudo-spectrum layer over an interactive line-identification tool. This tool was designed, among other applications, to obtain the "guess" redshift value once the emission features are identified. These steps prepare the ELS sample of interest, from which the final sample may be obtained.

3.3. Deconvolving pseudo-spectra of emission-line sources

After the ELS sample of interest has been established, the pseudo-spectra of these ELSs must be reduced by the

instrumental response, using the guess redshift as input, in order to obtain useful data for science exploitation.

The OTELO RTF instrumental transmission is well described by Eq. (5) in OTELO-I, and is represented in Fig. 1. As mentioned above, the effective passband ($\delta\lambda_e$) adopted for the RTF survey is about three times the scan sampling. Thus, each point of an OTELO pseudo-spectrum is the result of a particular convolution of the input SED in the defined spectral range of the survey.

Instead of a direct deconvolution of pseudo-spectra by the scan response function (with the possible divergence and accuracy problems inherent to these techniques), we search for the theoretical pseudo-spectrum that minimises the error-weighted difference with the observed one. This inversion of spectral profiles has been successfully tested by other authors in similar situations (e.g. Cedrés et al. 2013, in the case of the [S II] λ6717,6731 doublet emission of H II regions in large design galaxies). In the case of this survey, this can achieved by combining a flat, zero-slope continuum with a set of three-parameter Gaussian profiles (central wavelength, amplitude, and width) for each emission line previously identified in the pseudo-spectrum (Sect. 3.2), and then convolving this theoretical model with the instrumental response of OTELO.

The line width and central wavelength of a theoretical Gaussian profile (one for each emission line identified) vary in broad ranges that are conveniently binned to obtain measurement resolutions of $0.25\,\text{Å}$ and $10^{-4}(1+z)$, respectively. This redshift sampling provides an accuracy refinement of the guess value by a factor of approximately two after deconvolution, which is enough for the purposes of this work. The amplitude of these Gaussian profiles fluctuates in proportion to the flux error of the corresponding line peak in the pseudo-spectrum to be deconvolved. The initial value of the flux density of the continuum and the range within which this value varies in the synthetic spectra are obtained starting from the f_c and $\sigma_{\text{med,c}}$ values, respectively, which are defined in Sect. 3.

For a given observed pseudo-spectrum, a custom software application was used to perform the inverse deconvolution in the grid nodes of the above-defined parameter space. The theoretical spectrum associated with each jth node is convolved by the OTELO scan response, and the resulting pseudo-spectrum is compared with the observed one by means of the standard χ^2 statistics, defined by

$$\chi_j^2 = \sum_{i=1}^{N} \frac{(s_i - t_i)^2}{\sigma_i^2}, \qquad (1)$$

where the sum is over the N slices of the pseudo-spectrum, s_i and t_i are the observed and theoretical flux densities, respectively, and σ_i is the observed flux density error at the ith slice. We adopted the jth model parameter set with the minimum χ_j^2 as the formal result of the analysis.

We say that the deconvolution algorithm converges if a reliable theoretical spectrum is obtained from it, that is, if (i) the errors on the line fluxes obtained from the inverse deconvolution are below 50% of the line flux values, and (ii) the best theoretical continuum and EW of the line, or lines, are within the limits of the corresponding parameters obtained from the simulations described in Sect. 4. If both conditions are met, the ELS candidate becomes part of the final sample.

The parameter set given by the inverse deconvolution of the ELS candidates provides the best central wavelength of each emission line previously identified in the pseudo-spectrum and consequently a redshift estimation, z_{OTELO}. This procedure also

provides the best zero-slope continuum flux density and the parameters of the Gaussian function associated with each emission feature present in the pseudo-spectrum, allowing us in addition to determine the $m\,(<N)$ points of the pseudo-spectrum that contribute to each emission line. Using these data, the software application finally computes the net line flux by integrating the Gaussian profile obtained after χ^2 minimisation because each profile is independent of the continuum. The error of the line flux is the average χ_j^2 as defined by Eq. (1), but obtained over the points of the pseudo-spectrum that contribute to the particular emission line. This approach is valid as long as there are no blended emission lines involved, which is the case of this work.

Finally, the inverse deconvolution of the pseudo-spectra allows us to recover a line flux measure – even for the case of emission lines truncated by the spectral limits of the survey – as long as the peak of the emission feature is within this range. An example of this situation is shown in Fig. A.1.

4. Emission-line-source detection in OTELO from simulations

Source detection in NB emission-line surveys depends not only on the emission line flux (determined in the simplest case by the line width and intensity), but also on its strength relative to the continuum parametrised by the observed equivalent width (EW_{obs}).

We created synthetic spectra containing emission lines with Gaussian profiles distributed in a uniformly gridded parameter space driven by the width and the intensity (amplitude or core) of the line, as well as the flux density at the continuum. We then obtained simulated pseudo-spectra from the convolution of these synthetic spectra with the instrumental transmission of OTELO. These simulations aim to determine educated detection probabilities of ELSs for this survey. The limits of this parameter space are wide enough to contain the preliminary ELS set described in OTELO-I after the convolution of all the synthetic spectra. Thus, the width of the lines (in terms of FWHM) was varied between 1 and $100\,\text{Å}$ in steps of $\sim4\,\text{Å}$ ($200\,\text{km s}^{-1}$). The lower bound corresponds to a width of $\sim30\,\text{km s}^{-1}$ at the central wavelength of the RTF scan, and the upper bound to a very broad line of $\sim3300\,\text{km s}^{-1}$ at the rest-frame. The given range is representative of the likely cases from dwarf galaxies to some broad-line AGNs. Similarly, the flux densities S_λ [erg s^{-1} cm^{-2} Å^{-1}] of both the line intensity and the continuum of the synthetic spectra were uniformly binned in the range $-22.3 \leq \log S_\lambda \leq -16.3$ in order to widely sample the corresponding ranges of the preliminary ELSs of the survey.

Combined sky and photon noise per pixel was measured in 14 selected blank regions of 11×11 pixels whithin the background noise maps resulting from the analysis of the 36 OTELO RTF slices. The noise values for each slice were averaged, obtaining a spectrum of the OTELO tomography. This noise spectrum was resampled to the resolution of the synthetic spectra. Each element of the resulting noise spectrum was randomly modelled by a Gaussian distribution that approximates the noise behaviour, and was then added to the corresponding wavelength value in the synthetic spectrum.

After defining the line-width–intensity–continuum grid, a total of 500 independent synthetic spectra per grid node were obtained. Each synthetic spectrum was convolved with the instrumental response of the RTF scan defined in Sect. 2 in order to obtain the simulated pseudo-spectrum. For a given node of the grid we tested whether or not each of the 500 pseudo-spectra
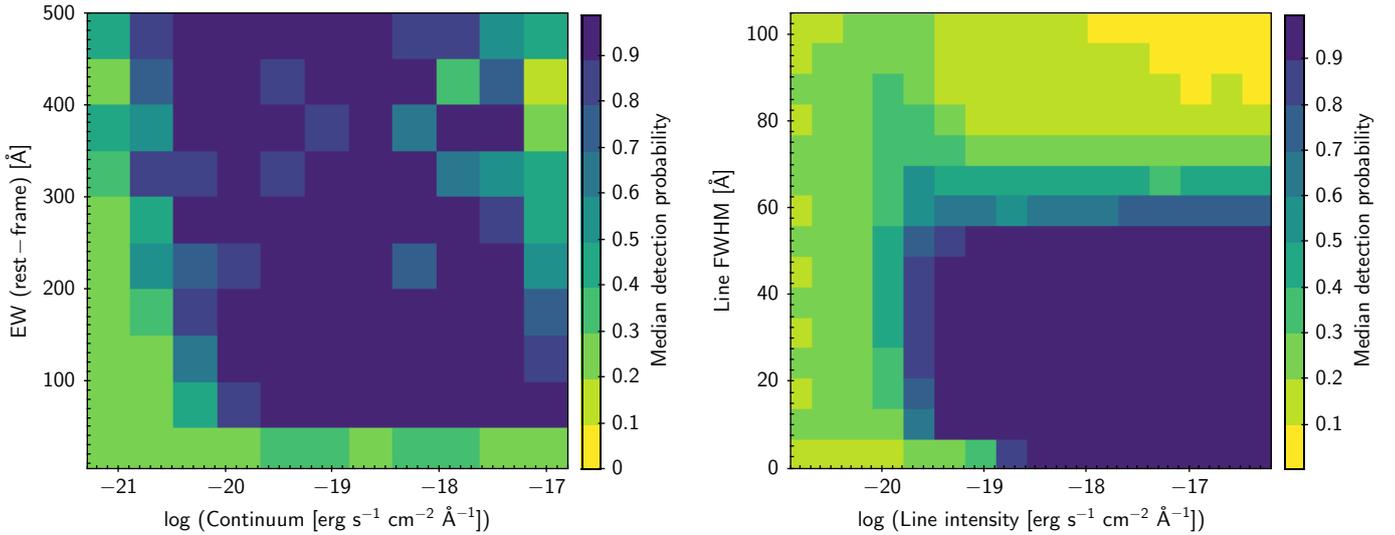
Fig. 2. Examples of detection probabilities of ELSs in OTELO from simulations. *Left*: median detected EW (rest-frame) as a function of the continuum in the input spectra resulting from simulations. *Right*: median value of detection probability in the line-width–intensity plane after the 500 runs of the simulations described in Sect. 4. The steep downturn of the median detection probability occurs when the emission-line width exceeds ~60 Å.

fulfilled the selection criteria given in Sect. 3. We assigned a value of "1" (or "0") whenever the line detection was made (or not) and averaged the results in each node. This mean value defines the detection probability function of the grid node in question, which depends on the line intensity, width, continuum flux density, and the rest-frame EW calculated from these parameters. As an example of the results, Fig. 2 (left) shows the detection probability distribution from the simulations in the EW (rest-frame)–continuum plane.

Data from simulations are also useful for obtaining relatively realistic emission-line flux distributions. Figure 2 (right) represents the detection probability distribution in the line-width–intensity plane, which allows us to calculate the required line flux statistics in each node of the simulation. Remarkably, this plot confirms that the ELS detection probability drops dramatically when the line width of a source exceeds ~60 Å. On the other hand, simulated data constitute the basis of the completeness correction in the LF calculation given in Sect. 6.

5. The case of [O III] ELSs at $\langle z \rangle = 0.83$

As mentioned above, the main aim of this work is to demonstrate the potential of OTELO by analysing a sample of [O III] ELSs at intermediate redshift. To this end, we first describe the implementation of the selection steps given in Sect. 3 in this particular science case, followed by relevant notes about the limitations of this selection method. Finally, the main properties of the final [O III] ELS sample are given.

5.1. Selecting the [O III] sample

According to the content of Sect. 3.2, we first defined $0.77 \leq z_{\mathrm{phot}} \leq 0.89$ as the redshift interval needed to safely include all [O III] ELS candidates. This range already takes into account the phase effect and the effective passband ($\delta\lambda_{\mathrm{e}}$) of the RTF slices at both ends of the scan, as well as the effect of the global accuracy of the photometric redshift estimations. Using the photo-z solutions that include the OTELO-Deep photometry, we found 401 preliminary [O III] ELS candidates within this

Table 2. Number of ELS candidates obtained from the selection process of the [O III] emitters.

ELS candidate subset	Number
[O III]	208
Hβ	56
He II $\lambda4686$	25
[N I] $\lambda5199$	6
[O III] $\lambda4363$	5
Total	300

z_{phot} range that meet the photo-z error condition also given in Sect. 3.2. To this set we added 140 preliminary ELS candidates whose observed SEDs were better fitted with `AGN/QSOs` templates than with the galaxy library (see OTELO-I).

The pseudo-spectra of the 541 resulting [O III] ELS candidates were examined individually in order to identify plausible emission lines and assign a guess redshift to the source. From these, a total of 300 ELS candidates attributable to different emission lines were found. In particular, the pseudo-spectra of 208 of these ELS candidates contained at least one of the [O III] $\lambda4959,5007$ features, and the emission feature in the pseudo-spectra of 92 candidates were assigned to neighbouring emission lines (see Table 2) based on the significance and the error estimation of the z_{phot} and the information provided by the pseudo-spectra. From the remaining 241 sources, 21 were discarded as probably spurious and 220 could not be classified as reliable ELS candidates owing to the presence of multiple unlikely features in their pseudo-spectra, in accordance with the requirements given in Sect. 3.2.

The pseudo-spectra of the 208 [O III] ELS candidates were deconvolved in order to obtain accurate redshifts (z_{OTELO}), continuum flux densities, and parameters for the emission lines(s) detected. The algorithm successfully converged for a total of 182 sources.

We make a comparison between the resulting redshifts from OTELO and those obtained from DEEP2 data. Catalogued DEEP2 redshifts with a quality flag $Q \geq 3$ (Newman et al. 2013)

are also available for a total of 26 of these latter-mentioned 182 sources. The Pearson correlation coefficient between spectroscopic redshifts from OTELO and DEEP2 surveys is 0.998, with no outliers. The mean accuracy of z_{OTELO} related to z_{DEEP2}, $|\Delta z|/(1 + z_{DEEP2}) \leq 2.54 \times 10^{-4}$. This value is consistent with the upper-limit error of z_{DEEP2} with $Q \geq 3$, which is on the order of $3 \times 10^{-4}/(1 + z_{DEEP2})$.

Representative examples of [O III] ELSs with a bright, faint, or very faint continuum, and their deconvolved pseudo-spectra, are shown in Fig. A.1. As also shown in this figure, the inverse deconvolution provides recovery of the emission line profile truncated by the edges of the spectral range of OTELO whenever the emission line peak was sampled in the pseudo-spectrum.

5.2. Contamination of the [O III] sample

Galaxy count statistics and other empirical estimations of cosmological parameters depend on the results of low-resolution emission-line galaxy (ELG) surveys that often contain foreground and background contaminants or interlopers due to misidentifications of spectral features (Hayashi et al. 2018; Grasshorn Gebhardt et al. 2019). In particular, a detailed estimation of the residual contaminants possibly present in the final sample of ELSs used in this work is a necessary but not sufficient condition for a reliable assessment of the LF([O III]).

The most common contaminants of NB surveys for the search of ELSs are the possible Balmer-jump sources, as well as the lower and higher redshift interlopers (see e.g. Hayashi et al. 2018) if the errors in photo-z are comparable to the differences between these redshifts and the one being sought. In the science case presented here, this class of contaminants is composed of misidentified Hα and [O II] $\lambda3726,3729$ ELSs at redshifts of ~0.4 and ~1.4, respectively. We also envisage, as an additional class of interlopers in OTELO, the ELS preliminary candidates selected on the basis of inadvertently incorrect photo-z estimations, despite their error values fulfilling the criteria given in Sect. 3.2. As mentioned above, the selection of ELSs in OTELO depends on the photo-z and the associated errors, as well as the identification of emission lines in pseudo-spectra above a given significance level.

The sample of [O III] $\lambda4959,5007$ ELSs previously obtained is free from Balmer-jump interlopers because the latter ones can easily be identified among the preliminary ELS candidates in the case where a misleading photo-z (see below) has allowed them to be included in the sample. Therefore, the degree of contamination of the final [O III] ELS sample is limited only to determine the balance of interlopers due to known line misidentifications and the likely fraction of sources with catastrophic photo-z (and reasonable errors) incorrectly assumed as [O III] ELS.

In order to reject redshift interlopers, we selected all the preliminary Hα and [O II] $\lambda3726,3729$ ELS candidates in OTELO whose photo-z estimations lie within $0.36 \leq z_{phot} \leq 0.42$ and $1.41 \leq z_{phot} \leq 1.55$, respectively. These sets contain the broadest selection of possible redshift interlopers present in the [O III] $\lambda4959,5007$ ELS sample obtained by following the steps described in Sect. 5.1. We then cross-correlated the [O III] $\lambda4959,5007$ ELS sample with each one of these sets. We found no Hα candidates in the [O III] $\lambda4959,5007$ sample from the diagnostics of the lower redshift interlopers. On the other hand, we found two possible [O II] $\lambda3726,3729$ interlopers (i.e. the OTELO sources ID: 03564 and 04264) after cross-correlation of the [O III] $\lambda4959,5007$ ELS sample with the preliminary [O II] $\lambda3726,3729$ ELS set. However, the source ID: 03564 is a [O III]$\lambda4959 +$ Hβ ELS, with $z_{DEEP2} = 0.8348$, and

the source ID: 04264 clearly exhibits the [O III] $\lambda4959,5007$ doublet in its pseudo-spectrum. Thus, the photo-z estimations of these sources differ from the true redshift. In both cases, high-resolution images from HST-ACS reveal the presence of sources with several knots inside the OTELO segmentation imprint. This fact suggests that the observed SED of such sources is of composite type and may not be necessarily well adjusted by the single galaxy templates used to estimate their photo-z. Regarding the results of this analysis, there are not indications of lower or higher redshift interlopers in the [O III] $\lambda4959,5007$ sample obtained as described in Sect. 5.

Finally, the adoption of the uncertainty limits on photo-z given in Sect. 3.2 ensures that ELS candidates with large errors are excluded from the final sample. However, there is a non-zero probability that some ELS candidates have been selected on the basis of catastrophic redshifts despite their moderated errors. Hence, and according to the established in OTELO-I, the fraction of these likely interlopers (δ_{cat-z}) up to $z \sim 1.4$ is at most 0.04. This statistical contamination effect is included in the error budget of the LF([O III]) formulated in Sect. 6.

5.3. The [O III] doublet and the missing emission-line sources

Depending on the signal-to-noise ratio of the emission lines, an [O III] $\lambda4959,5007$ source can be easily recognised in OTELO pseudo-spectra without additional information if both components of the doublet appear in it, because the characteristic ratio [O III]$\lambda4959$/[O III]$\lambda4959 \sim 0.3$ (Osterbrock & Ferland 2006). This distinctive feature can help to quantify the main bias of the ELS selection procedure used above in the practical case of [O III] and other chemical species.

Using the web-based GUI in a procedure completely separate from the [O III] ELS selection, all the pseudo-spectra were visually inspected to look exclusively for the [O III] doublet characteristic signature. We found 29 sources whose pseudo-spectra are fully compatible with the [O III] $\lambda4959,5007$ emission. All of these visually selected [O III] ELSs are included in the 182 [O III] obtained as described in Sect. 5.1 except for two [O III] emitters for which there are no detections in ancillary data because of their faintness at the continuum; this prevents any kind of z_{phot} estimation, and consequently such sources cannot be selected by the procedure described in Sect. 3. The inverse deconvolution of both of these latter two mentioned pseudo-spectra thoroughly converged, as expected, and these are shown in Fig. A.1. These bona fide [O III] $\lambda4959,5007$ sources were added to those from the standard selection process. In this way, the final set of [O III] ELSs in OTELO was found to contain 184 sources.

According to the emission features observed in the pseudo-spectra, a total of 84 ELSs show the [O III] $\lambda4959,5007$ doublet in their pseudo-spectra. The remaining 100 ELSs to complete the final set of [O III] ELSs in OTELO show either the [O III] $\lambda5007$ or the [O III]$\lambda4959$ emission line. For illustrative purposes, the OTELO pseudo-spectra are wide enough to contain the [O III]$\lambda4959$ and the Hβ lines near their extremities at the mean redshift of this science case. Thus, among the ELSs that only show the [O III]$\lambda4959$ component in their pseudo-spectra (34), we account for 23 ELSs that exhibit the [O III]$\lambda4959$ and Hβ pair. The study of the Hβ ELS sample in OTELO is the subject of a forthcoming contribution (Navarro et al., in prep.). Table 3 summarises the statistics of the subsets that integrate the final sample of [O III] ELSs, depending on the emission features found.

Table 3. Number counts in subsets that contribute to the final [O III] ELS sample of OTELO according to the features observed in their pseudo-spectra.

ELS subset	Number
[O III] $\lambda4959,5007$ (includes 2 ELSs missing in ancillary data)	84
[O III] $\lambda5007$ only	66
[O III] $\lambda4959$ only	11
[O III] $\lambda4959$ + Hβ	23
Total	184

Based on these number statistics on the [O III] ELS detections, the probability p_d of missing ELSs that show the [O III] doublet in OTELO is 2/84 or 2.4% if the ELS selection procedure described in Sect. 5.1 is followed without further add-ons. Under the same hypothesis, and considering a uniform distribution of emission lines in OTELO pseudo-spectra at $\langle z \rangle = 0.83$, the probability p_s of missing ELSs whose pseudo-spectra show either the [O III]$\lambda5007$ or the [O III]$\lambda4959$ emission line is around 2%. If these estimations are considered valid for any other emission line in OTELO, the probability of excluding a true ELS is $p_{doublet} + p_{single}$ or about 4.4%, because both events are disjointed. As mentioned, in the case considered in this paper this fraction drops to 2%, since we already added the two [O III] ELSs identified exclusively from pseudo-spectra inspection.

At last, it is worth pointing out that the error-weighted mean flux ratio $f([O\,III]\lambda4959)/f([O\,III]\lambda5007)$ of the 84 sources whose pseudo-spectrum shows the doublet is 0.328, with a standard deviation $\sigma = 0.229$. This mean ratio is constant below 1σ over the whole range of $EW_{obs}([O\,III]\lambda5007)$, which is in good agreement with the theoretical ratio given above, despite the dispersion of measured ratios increasing for lower EW_{obs}. Similar behaviour is reported in Boselli et al. (2013), who attribute some of the greatest deviations to AGN hosts with low EW([O III] $\lambda5007$). Hereafter, the [O III] line fluxes refer to [O III] $\lambda5007$, unless otherwise specified.

5.4. Main physical properties of [O III] emission line sources

From the previous analysis, the final OTELO sample of [O III] ELSs is distributed in the redshift range $0.78 \leq z_{OTELO} \leq 0.87$, with a mean $\langle z \rangle = 0.83$.

Figure 3 (left) shows the line flux and the EW_{obs} distributions of this set. The median values are 8.7×10^{-18} erg s^{-1} cm^{-2} and 45.7 Å, respectively. The [O III] ELS sample reaches a limiting line flux of 4.6×10^{-19} erg s^{-1} cm^{-2} and EW_{obs} as low as ~5.7 Å. These limits are consistent with those expected when derived from the simulations presented in Sect. 4, and both could be taken as representative values of the survey.

Figure 3 (right) shows the morphology and stellar mass distribution of the sources in the [O III] $\lambda4959,5007$ ELS set. From a visual and quantitative morphological analysis of OTELO sources (Nadolny et al., in prep.) using publicly available high-resolution images from *F814W*[3], 85% of the 127 classified sources (from the 184 ELSs of the final sample) are composed of disc-like galaxies. For 57 sources of this ELS sample the morphological classification was uncertain because of their exceedingly low signal level in the image, or were simply left

---

[3] http://aegis.ucolick.org/mosaic_page.htm

unclassified because they are outside the HST-ACS imprint. The visual classification of all sources up to $z_{phot} = 2$ is being performed by the OTELO Team and involve the use of MorphGUI, an application specially developed for this purpose by Kartaltepe et al. (2015), in the framework of CANDELS. A list of defined morphological classes is given in Fig. 3 (right).

We obtained stellar mass ($M_\star/M_\odot$) estimates for 171 of 184 [O III] $\lambda4959,5007$ ELSs (94%) using the relation of mass-to-light ratio with colour for star-forming (SF) galaxies at redshift $z < 1.5$ given in López-Sanjuan et al. (2019). Following this prescription we employed the rest-frame $(g–i)$ colour, together with absolute i-band magnitude for each source. The required data were computed from the available observed data in the OTELO multi-wavelength catalogue and the k-correction was provided by a SED-fitting of these photometric data at the redshift obtained from inverse deconvolution or z_{OTELO}. The reported dispersion of this mass-to-light ratio ($\sigma_{SF} = 0.9$) is slightly smaller than that obtained by Taylor et al. (2011) for galaxies from the GAMA survey, probably because of the addition of a quadratic colour term in such a relation. Therefore, based on this proxy, almost 87% of the 171 [O III] $\lambda4959,5007$ ELSs should belong to the low-mass galaxy population ($M_\star \lesssim 10^{10} M_\odot$). Furthermore, using the observational criterion given by Gil de Paz et al. (2003) for a galaxy to be classified as a blue compact dwarf (BCD; i.e. $M_K > 21$ mag), 74% of the [O III] ELS sample is composed of dwarf galaxies.

Finally, 31 (17%) of the 184 [O III] ELSs are infrared (IR) galaxies, based on the *Spitzer* and *Herschel* data fit using Chary & Elbaz (2001) IR SEDs (see OTELO-I for additional details). Their stellar masses are greater than $10^9 M_\odot$ and 11 of them qualify as luminous IR galaxies (LIRG: $10^{11} < L(\mathrm{TIR}\,[L_\odot]) < 10^{12}$).

6. The [O III] luminosity function

Using the data obtained from the analysis of the [O III] ELS set described, as well as suitable information from the simulations of the survey, we compute here the [O III] $\lambda4959,5007$ luminosity function, LF([O III]), of OTELO at $\langle z \rangle = 0.83$ after taking into account the main uncertainties and selection effects that could impact this calculation, which are described as follows.

6.1. Completeness of the [O III] sample

There are two main considerations to be made concerning the completeness of the final [O III] ELS sample. Firstly, the probability of excluding a true positive [O III] ELS because of its faintness at the continuum should be taken into account, as discussed in Sect. 5.3; this fraction, δ_{miss}, accounts for 2% of this particular ELS sample. Secondly, looking at the bounds imposed by data in the final sample, and based on emission-line object detectability simulations in the EW_{obs}–continuum binned space described in Sect. 4, we obtained mean values of the ELS detection probability (MDP) as a function of the [O III] line flux. This probability function was in turn modelled by a sigmoid algebraic function (similar in behaviour to the error function, erf), of the form

$$d = \frac{aF}{\sqrt{c + F^2}}, \qquad (2)$$

where $F = \log(f_l) + b$, f_l is the line flux, and $a = 0.972 \pm 0.007$, $b = 18.373 \pm 0.092$, and $c = 0.475 \pm 0.122$ are the parameters obtained from a weighted least-squares fit. This function was adopted as the completeness correction function (CCF) for calculations involving emission-line flux statistics at $z = 0.83$. The
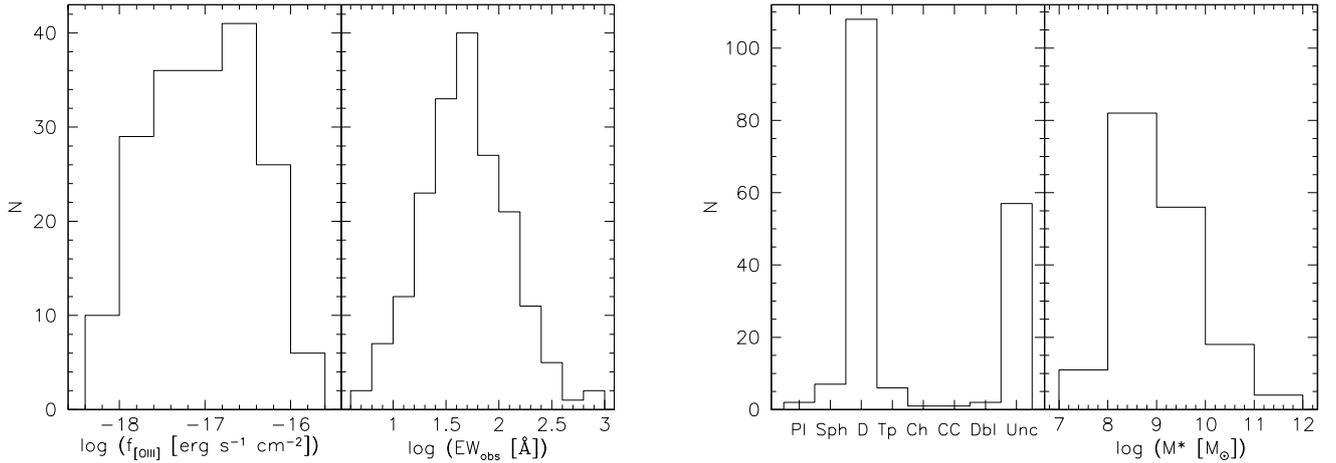
Fig. 3. Distribution of characteristic parameters of the OTELO [O III] sample. *Left*: [O III] line flux and observed EW measured in [O III] pseudo-spectra. Line flux and EW$_{obs}$ limits are $\sim 5 \times 10^{-19}$ erg s^{-1} cm^{-2} and ~ 6 Å. *Right*: morphology and stellar mass distribution of the OTELO [O III] ELS sample. The main morphological classes represented here are: Pl – Point-like; Sph – Spheroid; D – Disk; Tp- Tadpole; Ch – Chain; CC – Clumpy Cluster; Db – Doubles; Unc – Uncertain/Non-classified. At least 127 sources are disc-like galaxies and the median stellar mass is $8.36 \times 10^8\,M_\odot$. See main text for details.
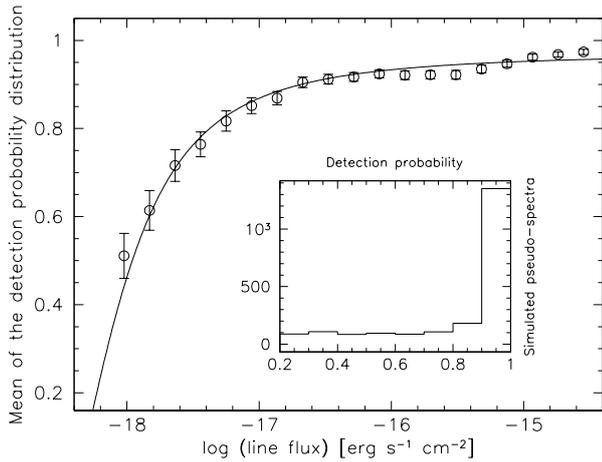
Fig. 4. Mean of the detection probability of the [O III] ELSs at $\langle z \rangle = 0.83$. The inset shows the detection probability distribution of all simulated pseudo-spectra described in Sect. 4 used to obtain the function represented here. The curve traces the least-squares weighted fit of the sigmoid function used to model such flux-binned mean values. Bars represent the mean standard error used for fit weighting.

CCF and its parent MDP distribution are shown in Fig. 4. The mean standard error of this distribution is $\delta_{\mathrm{MDP}} = 0.017$.

6.2. Cosmic variance

As a deep pencil-beam ($<1\,\deg^2$), single-pointing survey, the OTELO scan is affected by the relative cosmic variance (CV) at different levels, which can be ascribed to the effects of the underlying large-scale density fluctuations. In practice, this uncertainty depends on the mass (or luminosity) and the comoving volume sampled. Typically, CV is $\lesssim 10\%$ for a single volume of $10^7\,h_{0.7}^{-3}$ Mpc^3 projected onto an almost square sky region (Driver & Robotham 2010). In nearly all OTELO science cases, as addressed in this paper, the volumes explored are significantly smaller. Therefore, an estimate of the uncertainty due to the CV is imperative.

We estimated an uncertainty function due to the CV, $\sigma_{\mathrm{CV}}(M_\star)$ for eight bins in the stellar mass range $7.5 \leq \log$

$(M_\star/M_\odot) \leq 11.5$ for the [O III] sample, obtained as described in Sect. 5.4, by following the prescription of Moster et al. (2011). For practical purposes, the uncertainties obtained per mass bin were fitted by a three-parameter power law. To give a general idea of the CV effect, the mean uncertainty obtained for our ELS sample at $\langle z \rangle = 0.83$ is $\langle \sigma_{\mathrm{CV}} \rangle = 0.396$.

6.3. Survey volume

With regard to the phase effect mentioned in Sect. 3.2, for each [O III] ELS there is a corresponding passband with limits and width in wavelength (and hence redshift) that depends on the position of the source with respect to the optical centre of the RTF. Thus, with a redshift range for each source as a function of the radial distance to the optical centre (e.g. such as the top-hat profile shown in Fig. 1), and taking into account the effective passband $\delta\lambda_{\mathrm{e}}$ of the RTF in a single slice, we obtained the maximum comoving volume in which the emission line(s) of such sources can be detected. The comoving volumes range from 6708.9 (for a hypothetical source at the optical centre) to 6540.3 Mpc^3 (for a source located at $r_{\max}$). The comoving volume at a radius that divides the field of view into two equal angular surfaces is 6633.4 Mpc^3, and this is the value adopted as representative of the [O III] survey volume in Table 4. The effect of the wavelength accuracy of the RTF (see Table 1) on comoving volume calculations is negligible.

6.4. Luminosity function estimation

The [O III] luminosity of each ELS of the sample is given by $L([\mathrm{O\,III}]) = 4\pi f_{[\mathrm{O\,III}]} D_{\mathrm{L}}^2$, where $f_{[\mathrm{O\,III}]}$ is the [O III] flux obtained from the inverse deconvolution of the pseudo-spectrum (i.e. with no correction for dust attenuation in the galaxy), and D_{L} is the luminosity distance. The [O III] luminosity was distributed in the range $39.2 \leq \log L([\mathrm{O\,III}])\,[\mathrm{erg\,s^{-1}}] \leq 42.0$.

The first task for the LF calculation is to compute the number Φ of galaxies per unit volume (V) and per unit [O III]-luminosity $\log L([\mathrm{O\,III}])$. In this case, this number is provided by

$$\Phi[\log L([\mathrm{O\,III}])] = \frac{4\pi}{\Omega} \Delta[\log L([\mathrm{O\,III}])]^{-1} \sum_i \frac{1}{V_i\,d_i}, \qquad (3)$$

Table 4. Binned values of the observed [O III] luminosity function obtained from Eq. (3).

log L([O III]) [erg s^{-1}]	log ϕ [Mpc^{-3} dex^{-1}]	Number of [O III] ELSs
39.4	$-1.626^{+0.151}_{-0.234}$	14
39.8	$-1.758^{+0.136}_{-0.200}$	30
40.2	$-1.709^{+0.133}_{-0.192}$	42
40.6	$-1.836^{+0.136}_{-0.198}$	34
41.0	$-1.760^{+0.134}_{-0.195}$	42
41.4	$-2.161^{+0.150}_{-0.230}$	17
41.8	$-2.698^{+0.194}_{-0.359}$	5

Notes. Uncertainties correspond to the total errors described in the text. The last column contains the observed number (i.e. before completeness correction) of the [O III] ELSs in each luminosity bin.

where d_i is the detection probability given by the CCF, V_i is the comoving volume for the ith source, Ω is the surveyed solid angle (4.7×10^{-6} str), and $\Delta[\log L([\text{O III}])] = 0.4$ is the adopted luminosity binning.

Instead of using methods of measured data re-sampling, we adopt a scheme of error propagation based on the potential sources of uncertainty described in the preceding sections. The L([O III]) bins were treated independently. Estimation of the total error per bin as given in Table 4 was done as follows.

The main uncertainties that affect the LF([O III]) are those linked to the hypothesis of a Poisson point process in the galaxy distribution, which depends on the number of ELSs per L([O III]) bin and the effects of the CV (σ_{CV}). The total error per bin also includes the contributions of (i) the mean standard error of the completeness correction (δ_{MDP}), (ii) the false-positive detection rate of [O III] ELSs ($\delta_{\alpha-1}$), (iii) the probability of incorrect ELS identification ($\delta_{\text{cat}-z}$), and (iv) the lost [O III] ELS fraction due to a selection method based in part on broadband photometric data (δ_{miss}). The contributions of these errors were summed in quadrature and they are given in Table 4, along with the LF([O III]) values obtained from Eq. (3).

The Schechter (1976) function is the formalism adopted here to describe the luminosity function, $\phi(L) \, dL = \Phi[\log L([\text{O III}])] \, d(\log L)$, which is defined by

$$\phi(L) \, dL = \phi^*(L/L^*)^\alpha \exp(-L/L^*) \, d(L/L^*). \tag{4}$$

The parameter L^* is the characteristic value that separates the high(exponential)- and low(power-law)- luminosity regimes in the LF driven by ϕ^* and α, which are the number density at L^* and slope of the faint end of the function, respectively. This parametrisation facilitates the calculation of the luminosity and number density of the galaxies involved, as well as a partitioned comparison of different results. Thus, a Schechter function was fitted to the completeness-corrected data given in Table 4 using a least-squares minimisation algorithm based on the Levenberg–Marquardt method. The parameters obtained from the completeness-corrected LFs reported during recent years are summarised in Table 5.

Data from Ly et al. (2007) correspond to an NB survey of almost a dozen redshift windows between $z = 0.07$ and 1.47 explored in the Subaru Deep Field (SDF; Kashikawa et al. 2004). Using a maximum-likelihood analysis, Drake et al. (2013) derived an LF([O III]) from NB-selected ELSs in the Subaru/*XMM-Newton* Deep Field Survey (SXDS; Furusawa

et al. 2008), employing the NB921 filter of the Suprime-Cam on the 8.2 m Subaru Telescope. The most recent estimate of the LF([O III]) at $z \sim 0.8$ comes from the first Public Data Release of the HSC-SSP (Hayashi et al. 2018). This is a comprehensive NB imaging survey of ELSs at $z < 1.5$ observed using the NB921 filter with the same telescope. Their LF parameters were obtained from a combination of data over five extragalactic fields covering 16.2 deg^2 in total. The resulting LF for our [O III] ELS sample is shown in the Fig. 5 beside the plots of those obtained by the cited authors.

7. Discussion

As stated above, uncertainties on the LF([O III]) due to CV (intrinsically induced by density fluctuations and galaxy clustering) are greater with increasing stellar mass and decreasing survey area for the same redshift range. Apart from the covariance of the characteristic luminosity L^* with the LF normalisation ϕ^*, errors on this latter parameter are also affected by the CV. All these uncertainties contribute to the inaccuracies of the LF bright-end predictions (Wolf et al. 2003). At the faint end, the completeness corrections become more important as the luminosity data reach the detection limits, whereas the CV effects are more limited.

The largest relative uncertainty on the Schechter parameters obtained after the non-linear fitting of the OTELO LF([O III]) corresponds to the normalisation of the function ($\delta_r \phi^* = 25.5\%$), followed by that of the characteristic luminosity ($\delta_r L^* = 18.2\%$). The inset in Fig. 5 shows the strong correlation between both parameters. The relative error of the faint-end slope $\delta_r \alpha$ obtained is about 6.6%.

Despite the difficulty in comparing Schechter-LFs because the parameters are more or less correlated, a general agreement can be observed between the LF estimates from previous studies and those of OTELO at $\log L([\text{O III}]) \approx 42$. However, the OTELO LF([O III]) prediction in the vicinity of L^* is $\sim$0.3 dex greater than those of Ly et al. (2007) and Drake et al. (2013), and is about 0.6 dex greater than the model of Hayashi et al. (2018). Assuming a similar covariance of the LF normalisation with L^* for all cases considered here, we attribute such offsets to the differences between the normalisation parameters and their uncertainties, which as indicated above could be mainly related to the CV effects. Indeed, the fitted ϕ^* values tend to become smaller as the order of magnitude of cosmic volume explored is greater. The volume sampled by OTELO is approximately 7 and 1000 times smaller than those explored in previous studies. From the work of Hayashi et al. (2018) in particular, it is evident that the combination of five different samples of ELSs in a cosmic volume up to $\sim$10^6 Mpc^{-3} not only allows mitigation of the small-number statistics affecting the LF bright-end, but also substantial reduction of the uncertainties linked to the CV, despite their significant relative errors on the parameters ϕ^* and L^*. In summary, the volumes sampled by the authors cited here make their LF estimations more proficient than OTELO in sampling the bright side of the LF([O III]). Interestingly, the upper envelope of the LFs represented in Fig. 5 suggests that a double power-law function might better represents the bright side, as noted in recent investigations related to number statistics of ELGs (see Comparat et al. 2016, and references therein).

Even more remarkable is the behaviour of the LFs listed in Table 5 at low luminosities. As a result of the combined effect of the line flux limit and EW$_{\text{obs}}$ reached by OTELO, the LF reported in this work extends to luminosities that are about ten times fainter than the most sensitive observations of this kind made
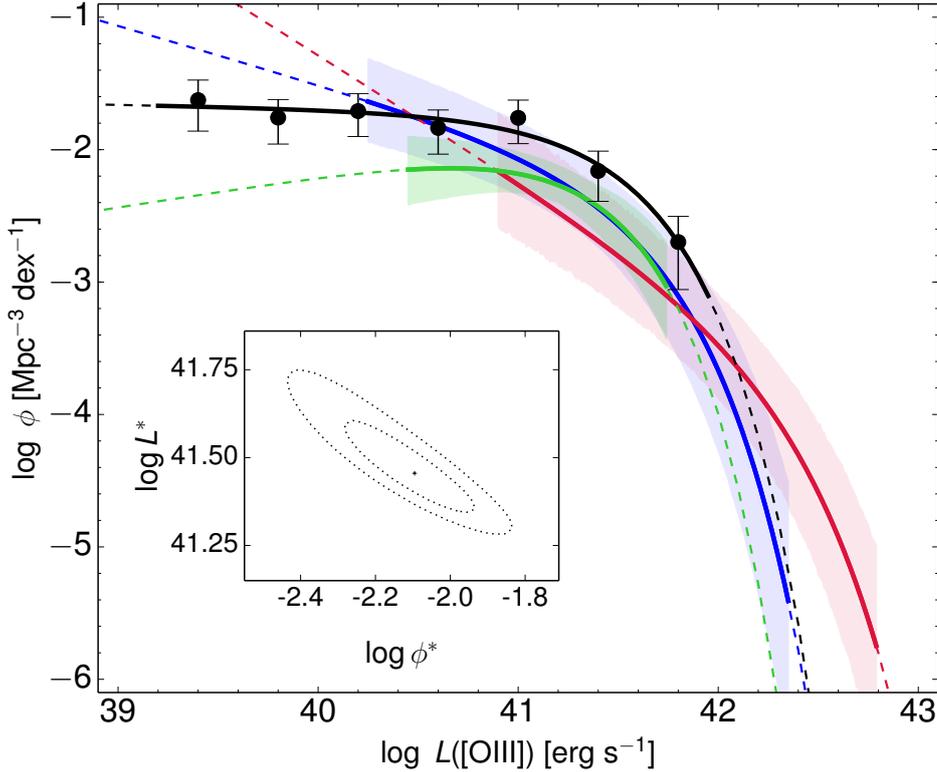
Fig. 5. Completeness-corrected [O III] luminosity functions at $\langle z \rangle \sim 0.8$ from the recent literature and OTELO survey data. The observed (i.e. with no correction by dust attenuation) LFs of Ly et al. (2007), Drake et al. (2013), Hayashi et al. (2018) are plotted in blue, green, and red, respectively. In each case, the solid line extends over the sampled luminosities in each survey, while the dashed line is the extrapolation of the corresponding best fit. The colour-shaded areas depict the propagated uncertainties of the cited LFs. The black curve represents the best fit of the Schechter function to the OTELO LF([O III]) data (dots). Error bars are the result of the LF uncertainty scheme per bin as detailed in Sect. 6.4. The relevant data for this LF are given in Table 4. The inset shows the 68% and 90% confidence contours for the OTELO data fit in the space of the parameters that show the largest uncertainties (see text).

Table 5. Best-fit Schechter parameters for [O III] observed LFs extracted from the literature and the best fit of the OTELO LF([O III]) data given in Table 4.

Dataset	Method	Number of sources	Mean redshift	Volume [10^3 Mpc^3]	$\log \phi^*$ [Mpc^{-3} dex^{-1}]	$\log L^*$ [erg s^{-1}]	α	$\log L_{\min}$ [erg s^{-1}]	$\log L_{\max}$ [erg s^{-1}]
Ly et al. (2007)	NB	662	0.84	43.65	-2.54 ± 0.15	41.53 ± 0.11	-1.44 ± 0.09	40.25	42.36
Drake et al. (2013)	NB	910	0.83	123.50	$-2.25^{+0.07}_{-0.09}$	$41.28^{+0.07}_{-0.08}$	$-0.76^{+0.22}_{-0.19}$	40.45	41.75
Hayashi et al. (2018)	NB	6428	0.84	460–6300 [a]	-3.71 ± 0.21	42.17 ± 0.11	-1.95 ± 0.11	40.9	42.8
This work	NB scan	184	0.83	6.63	-2.10 ± 0.11	41.46 ± 0.09	-1.03 ± 0.08	39.2	42.0

Notes. [a] Value calculated using data from five extragalactic fields.

to date, yielding a direct constraint on the faint-end slope with a moderate relative error. This α value is shallower than those found by Ly et al. (2007) and Hayashi et al. (2018), but steeper than that reported by Drake et al. (2013); all of them resulting from NB data obtained with the same instrumental setup, but surveying different sky fields. As established in Sect. 6.1, a careful completeness correction of the observed [O III] LF (Table 4) based on well-informed simulations was performed before the Schechter function fitting. The mean uncertainty on the CCF is not sufficient to explain these differences. Below, after an additional impact analysis of all LFs regarded in this work, we explore some possibilities and physical scenarios that could help to account for different α values.

To further contrast the outcomes of the [O III] LFs, we calculate the luminosity density $\mathfrak{L}([OIII])$ and the space density $\mathfrak{N}([OIII])$ of [O III] ELSs, after a numerical integration over the $39 \leq \log L([OIII])$ [erg s^{-1}] ≤ 43 luminosity range, which is roughly the same as that represented in the horizontal axis of Fig. 5. An estimation of the error on each integration was obtained from Monte Carlo analysis with 10 000 realisations, assuming a normal distribution of the errors of the Schechter parameters given in Table 6. In Table 6 we show the resulting densities and their errors corresponding to each survey, as well

as the mean values (μ) and the standard deviations (σ_μ) of these density calculations.

As expected, and despite the discrepancies between LF parameters, the luminosity densities obtained are relatively self-consistent. Indeed, the standard deviation of the mean luminosity density is comparable to each uncertainty of $\mathfrak{L}([OIII])$. In contrast, the number densities estimated over the same luminosity range show mutual divergences by a factor of between 3 and approximately 20, precisely because of the dispersion in the behaviour of the predicted or observed LFs on the faint side. Therefore, the faint-end slope of these LFs has a limited impact on the estimation of $\mathfrak{L}([OIII])$ (see also Drake et al. 2013), but a powerful effect on the number density of ELSs.

From a causal analysis, there are computational, statistical, and physical effects that could contribute to the scatter of the faint-end slopes of the LFs of SFGs. For instance, the analysis of the LF(UV) at $z \approx 2$ reported by Parsa et al. (2016) suggests that a robust faint-end slope estimate requires good sampling of the LF extending as far below $\log L^*$ as possible. These latter authors demonstrated that there exists a dependence of the α value in the best-fitting Schechter LF on the limiting absolute magnitude down to which this fit is performed, meaning that brighter limits tend to give steeper slopes. Alternatively, Drake et al. (2013) not

Table 6. Luminosity $\mathfrak{L}$ and number $\mathfrak{N}$ densities of [O III] ELSs calculated from the numerical integration of the observed LFs given in Table 5, over the $39 \leq \log L(\text{[OIII]}) \,[\text{erg s}^{-1}] \leq 43$ luminosity range, as described in the main text.

Dataset	$\log \mathfrak{L}(\text{[OIII]})$ [erg s^{-1}]	$\log \mathfrak{N}(\text{[OIII]})$ [Mpc^{-3}]
Ly et al. (2007)	39.18 ± 0.20	-1.124 ± 0.228
Drake et al. (2013)	39.00 ± 0.12	-1.812 ± 0.205
Hayashi et al. (2018)	39.22 ± 0.30	-0.676 ± 0.381
This work	39.37 ± 0.14	-1.351 ± 0.153
μ	39.19 ± 0.10	-1.241 ± 0.128
σ_μ	0.13	0.410

Notes. The mean values (μ) and the standard deviations (σ_μ) of these density parameters are given in the rows at the bottom.

only claim that the detection fraction of ELSs plays an important role in the determination of the faint-end slope, but that this value is sensitive to the adopted limit of EW for the same faintest limit magnitude of a typical NB survey, which is on the order of the filter width. Based on this claim, and taking into account the EW lower limit of OTELO ELS data, namely about 6 Å, the faint-end slope provided in this work is more robust than that obtained from the analysis of classic NB data.

In addition, Drake et al. (2013) also found that values of α for a given redshift could differ significantly, depending on the different emission lines used for the LF estimate. In this sense, Sobral et al. (2013) examined the behaviour of α by consistently using Hα ELSs observed in different redshift slices at $0.4 < z < 2.23$, and contrary to a steepening with redshift found in other works, they reported a relatively non-evolving value $\alpha = 1.60 \pm 0.08$. In particular, Ly et al. (2007) argues that even with robust completeness correction, there is an intrinsic redshift evolution of the faint end of the star-forming galaxies towards a flatter slope. These latter authors also suggest that the faint end of the LF at $0.8 \lesssim z \lesssim 1.5$ estimated from NB data could be affected to some degree by improper identification of [O II] $\lambda3726,3729$ and [O III] ELSs (in their case, by less than 10%). Thus, misidentified lines could artificially contribute to increasing α values for a given redshift. As established in Sect. 5.2, the final sample of [O III] ELS described in this work is not declaredly affected by this kind of contamination.

Concerning the physical scenarios, Veilleux et al. (2005) suggest that the faint end of the LF flattens as an effect of the galactic winds produced by photo-evaporation in dwarf galaxies. The relatively shallow potential of such galaxies is in agreement with this hypothesis. On the other hand, there are alternative energetic mechanisms (AGNs and SNe) that could explain the ionised gas outflows and feedback, each entailing galaxy cooling, intergalactic medium (IGM) enrichment, and star-formation suppression (Yuma et al. 2017). In the particular case of galaxies that dominate the $L \ll L^*$ regime, not only are supernova-driven winds able to explain the metallicities of dwarf galaxies, but the UV and X-ray backgrounds might also heat the IGM (see Guo et al. 2011, and references therein). In both cases, a reduction in star formation may be expected. For these reasons, Gargiulo et al. (2015) claim that among the possible mechanisms (within the framework of the Λ-CDM paradigm) that regulate the faint-end slope of the LF in SFGs, both the rate of SNe (which depends on galaxy mass; in particular, the core-collapse type) and the efficiency of SNe feedback in the bulge and in the disc are of particular relevance. These effects can be

introduced as free parameters for example in the semi-analytic models of galaxy formation. In this sense, OTELO provides data for the fine tuning of these parameters.

Finally, from an evolutionary point of view, these phenomena would explain the flattening of the LFs of SFGs since cosmic epochs similar to or earlier than those explored in this paper, and force the galaxy to evolve towards low-mass early types (dEs) that populate both cluster (Aguerri 2016) and field (Sybilska et al. 2018) environments in the Local Universe. Under this general assumption, a fraction of the galaxies that contribute to the OTELO LF([O III]) could be predecessors of local post-starbursts and dEs.

8. Summary

The OTELO survey is a new NB imaging survey that covers a $7.5' \times 7.4'$ ($\sim$0.015 square degree) area in the EGS field. Using the RTF of the OSIRIS instrument on the GTC, a spectral window of 230 Å in width, centred at $\sim$9170 Å, and reasonably free from strong sky emission lines was scanned with 36 evenly spaced (every 6 Å) slices, each of 12 Å in width. From this spectral tomography we obtained low-resolution pseudo-spectra of all the sources detected on the coaddition of the slices. These sources are listed in a custom multi-wavelength catalogue which was built using public broad-band ancillary data gathered within the framework of the AEGIS Collaboration. This catalogue contains a total of 9862 sources at 50% completeness magnitude of 26.38, and first-hand photometric redshift information with an uncertainty δz_{phot} better than $0.2\,(1 + z_{\text{phot}})$ is available for 6660 of them. Details of the survey strategy, data reduction, and main products are provided in OTELO-I.

Here, we demonstrate the scientific potential of the OTELO survey in a specific case for the selection of an ELS sample to unprecedentedly low limits in line luminosity.

For this purpose we first established a general procedure for ELS selection using OTELO data. From extensive simulations using synthetic pseudo-spectra, we estimated the limits of the survey in terms of emission line width, EW, and flux as a function of detection probability. These simulations allow us to derive a completeness correction for the LF determination and other survey biases.

The selection procedure was applied to the science case of [O III] $\lambda4959,5007$ ELSs. A total of 541 preliminary ELSs in the redshift window around $z = 0.8$ were examined. Of these, a total of 184 sources constitute the final [O III] ELS sample and another 92 from this preliminary set were classified as Hβ, He II $\lambda4686$, [N I] $\lambda5199$, or [O III] $\lambda4363$ ELS candidates (which are being used for further papers). After inverse deconvolution of their emission lines, accurate redshifts, line fluxes, and observed EWs were determined for the final [O III] ELS sample, which is distributed in the range $0.78 \leq z_{\text{OTELO}} \leq 0.87$, with a mean $\langle z \rangle = 0.83$. The vast majority (85%) of the morphologically classified [O III] ELSs are disc-like sources, and 87% of this sample have a stellar mass $M_\star < 10^{10}\,M_\odot$. In a complementary manner, almost three quarters of the ELSs of this sample are dwarf galaxies. A limiting line flux of $\sim$5 × 10^{-19} erg s^{-1} cm^2 and observed EWs as low as $\sim$6 Å were measured, which can be adopted as characteristic values of the survey as a whole. This validates the use of the TFs and the NB-scan technique for finding faint populations of SFGs, and in our opinion puts OTELO in a competitive position as the most sensitive survey to date in terms of minimum line flux and EW.

Sampling a comoving volume of $\sim$7 × 10^3 Mpc^3, and after analysing the contribution of the most important uncertainties,

we obtain an observed (i.e. with no correction for dust attenuation) LF from the final [O III] ELS sample that is ten times fainter than the faintest extreme reached by other surveys; its best fits delivered the following Schechter parameters: $\log \phi^* = -2.10 \pm 0.11$, $\log L^* = 41.46 \pm 0.09$, and $\alpha = -1.03 \pm 0.08$. This faint-end slope value provides a new constraint on the behaviour of the LF([O III]) and the number density of [O III] ELSs at redshift $z = 0.83$, despite the agreement of the LF obtained with recent literature data in terms of the integrated [O III] luminosity. In this sense, OTELO is complementary to other surveys with similar science goals and can help to put constraints on the parameters that regulate the statistics of dwarf SFGs in current models of galaxy evolution, specifically those dealing with feedback phenomena.

References

Álvarez, P., Rodríguez Espinosa, J. M., & Sánchez, F. 1998, New Astron. Rev., 42, 553

Aguerri, J. A. L. 2016, A&A, 587, A111

Arp, H. 1966, ApJS, 14, 1

Arnouts, S., Cristiani, S., Moscardini, L., et al. 1999, MNRAS, 310, 540

Benitez, N., Dupke, R., Moles, M., et al. 2014, ArXiv e-prints [arXiv:1403.5237]

Benson, A. J., Bower, R. G., Frenk, C. S., et al. 2003, ApJ, 599, 38

Bielby, R., Hudelot, P., McCracken, H. J., et al. 2012, A&A, 545, A23

Bongiovanni, Á., Ramón-Pérez, M., Pérez García, A. M., et al. 2019, A&A, 631, A9

Boselli, A., Hughes, T. M., Cortese, L., Gavazzi, G., & Buat, V. 2013, A&A, 550, A114

Bothwell, M. S., Kennicutt, R. C., Johnson, B. D., et al. 2011, MNRAS, 415, 1815

Brough, S., Hopkins, A. M., Sharp, R. G., et al. 2011, MNRAS, 413, 1236

Cedrés, B., Beckman, J. E., Bongiovanni, Á., et al. 2013, ApJ, 765, L24

Chary, R., & Elbaz, D. 2001, ApJ, 556, 562

Comparat, J., Zhu, G., Gonzalez-Perez, V., et al. 2016, MNRAS, 461, 1076

Damjanov, I., Zahid, H. J., Geller, M. J., et al. 2018, ApJS, 234, 21

Danieli, S., van Dokkum, P., & Conroy, C. 2018, ApJ, 856, 69

Dark Energy Survey Collaboration (Abbott, T., et al.) 2016, MNRAS, 460, 1270

Davis, M., Guhathakurta, P., Konidaris, N. P., et al. 2007, ApJ, 660, L1

Davies, L. J. M., Robotham, A. S. G., Driver, S. P., et al. 2018, MNRAS, 480, 768

Dawson, K. S., Kneib, J.-P., Percival, W. J., et al. 2016, AJ, 151, 44

De Lucia, G., Muzzin, A., & Weinmann, S. 2014, New Astron. Rev., 62, 1

Drake, A. B., Simpson, C., Collins, C. A., et al. 2013, MNRAS, 433, 796

Dressler, A., Spergel, D., Mountain, M., et al. 2012, ArXiv e-prints [arXiv:1210.7809]

Driver, S. P., & Robotham, A. S. G. 2010, MNRAS, 407, 2131

Driver, S. P., Norberg, P., Baldry, I. K., et al. 2009, Astron. Geophys., 50, 12

Driver, S. P., Davies, L. J., Meyer, M., et al. 2016, The Universe of Digital Sky Surveys, 42, 205

Furusawa, H., Kosugi, G., Akiyama, M., et al. 2008, ApJS, 176, 1

Gargiulo, I. D., Cora, S. A., Padilla, N. D., et al. 2015, MNRAS, 446, 3820

Gil de Paz, A., Madore, B. F., & Pevunova, O. 2003, ApJS, 147, 29

Grasshorn Gebhardt, H. S., Jeong, D., Awan, H., et al. 2019, ApJ, 876, 32

Guo, Q., White, S., Boylan-Kolchin, M., et al. 2011, MNRAS, 413, 101

Hayashi, M., Tanaka, M., Shimakawa, R., et al. 2018, PASJ, 70, S17

Ilbert, O., Arnouts, S., McCracken, H. J., et al. 2006, A&A, 457, 841

Kartaltepe, J. S., Mozena, M., Kocevski, D., et al. 2015, ApJS, 221, 11

Kashikawa, N., Shimasaku, K., Yasuda, N., et al. 2004, PASJ, 56, 1011

Klypin, A., Karachentsev, I., Makarov, D., et al. 2015, MNRAS, 454, 1798

Laureijs, R., Amiaux, J., Arduini, S., et al. 2011, ArXiv e-prints [arXiv:1110.3193]

Le Fèvre, O., Vettolani, G., Paltani, S., et al. 2004, A&A, 428, 1043

Lilly, S. J., Le Fèvre, O., Renzini, A., et al. 2007, ApJS, 172, 70

López-Sanjuan, C., Díaz-García, L. A., Cenarro, A. J., et al. 2019, A&A, 622, A51

LSST Science Collaboration (Abell, P. A., et al.) 2009, ArXiv e-prints [arXiv:0912.0201]

Lutz, D., Poglitsch, A., Altieri, B., et al. 2011, A&A, 532, A90

Ly, C., Malkan, M. A., Kashikawa, N., et al. 2007, ApJ, 657, 738

McLure, R. J., Pentericci, L., Cimatti, A., et al. 2018, MNRAS, 479, 25

Moles, M., Benítez, N., Aguerri, J. A. L., et al. 2008, AJ, 136, 1325

Moster, B. P., Somerville, R. S., Newman, J. A., & Rix, H.-W. 2011, ApJ, 731, 113

Newman, J. A., Cooper, M. C., Davis, M., et al. 2013, ApJS, 208, 5

Osterbrock, D. E., & Ferland, G. J. 2006, Astrophysics of Gaseous Nebulae and Active Galactic Nuclei, 2nd edn. (Sausalito, CA: University Science Books)

Parsa, S., Dunlop, J. S., McLure, R. J., & Mortlock, A. 2016, MNRAS, 456, 3194

Pascual, S., Gallego, J., & Zamorano, J. 2007, PASP, 119, 30

Pérez-González, P. G., Cava, A., Barro, G., et al. 2013, ApJ, 762, 46

Sánchez-Portal, M., Pintos-Castro, I., Pérez-Martínez, R., et al. 2015, A&A, 578, A30

Sandage, A. 1961, The Hubble Atlas of Galaxies (Washington: Carnegie Institution)

Schechter, P. 1976, ApJ, 203, 297

Scodeggio, M., Guzzo, L., Garilli, B., et al. 2018, A&A, 609, A84

Sobral, D., Smail, I., Best, P. N., et al. 2013, MNRAS, 428, 1128

Sobral, D., Matthee, J., Best, P. N., et al. 2015, MNRAS, 451, 2303

Somerville, R. S., & Primack, J. R. 1999, MNRAS, 310, 1087

Somerville, R. S., Gilmore, R. C., Primack, J. R., et al. 2012, MNRAS, 423, 1992

Stasińska, G. 2007, ArXiv e-prints [arXiv:0704.0348]

Strauss, M. A., Weinberg, D. H., Lupton, R. H., et al. 2002, AJ, 124, 1810

Suzuki, T. L., Kodama, T., Sobral, D., et al. 2016, MNRAS, 462, 181

Sybilska, A., Kuntschner, H., van de Ven, G., et al. 2018, MNRAS, 476, 4501

Taylor, E. N., Hopkins, A. M., Baldry, I. K., et al. 2011, MNRAS, 418, 1587

Veilleux, S., Cecil, G., & Bland-Hawthorn, J. 2005, ARA&A, 43, 769

White, S. D. M., & Frenk, C. S. 1991, ApJ, 379, 52

Wolf, C., Meisenheimer, K., Rix, H.-W., et al. 2003, A&A, 401, 73

Yoachim, P., Graham, M., Bet, S., et al. 2019, BAAS, 51, 303

Yuma, S., Ouchi, M., Drake, A. B., et al. 2017, ApJ, 841, 93
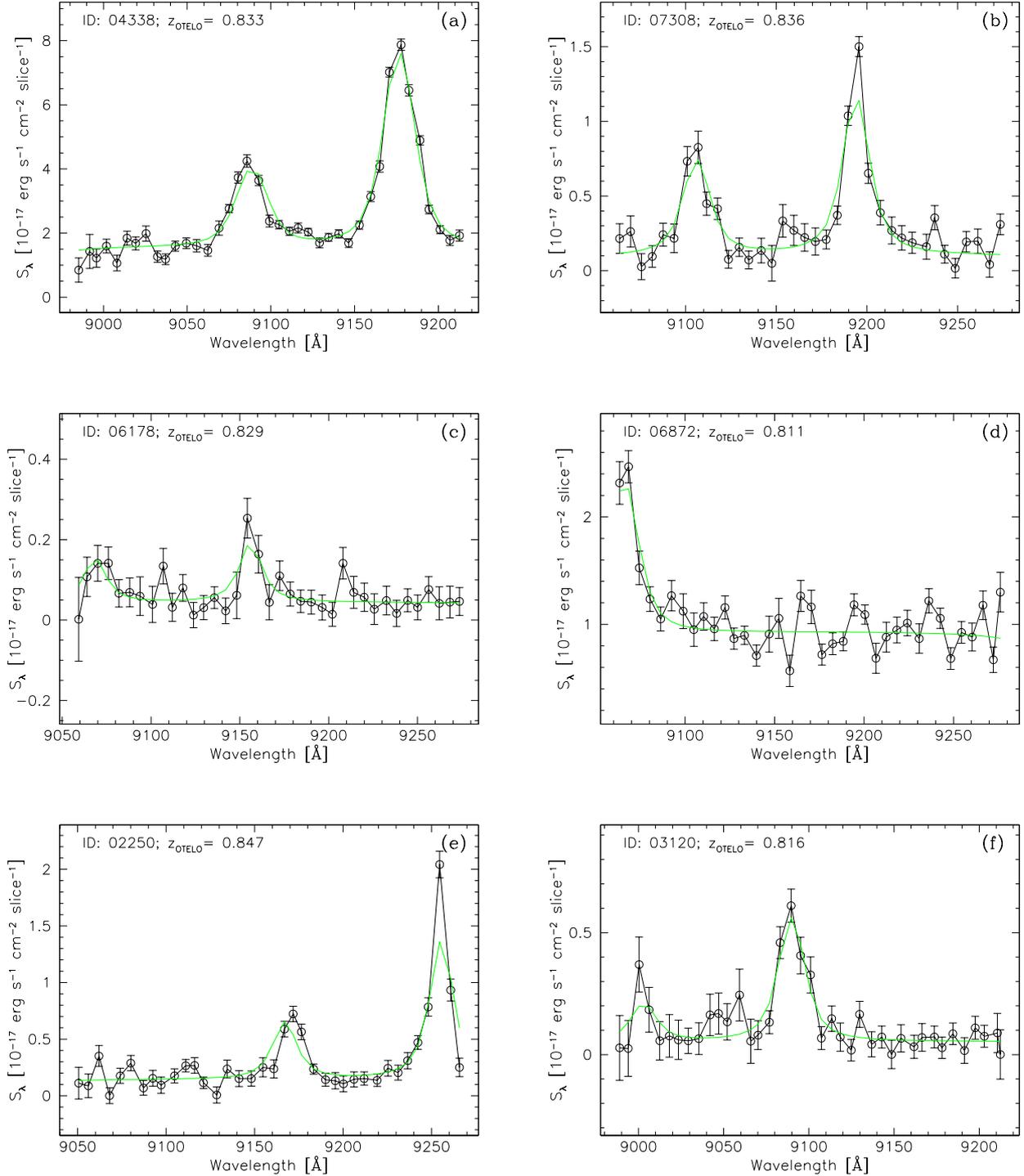
Appendix A: Examples of [O III] ELS

Fig. A.1. Examples of OTELO pseudo-spectra of [O III] sources (open circles). The best theoretical pseudo-spectrum obtained from the inverse deconvolution process described in Sect. 3.3 is represented by the green line. *Panels a–c*: pseudo-spectra with a bright (ID: 04338), a faint (ID: 07308), and a very faint (ID: 06178) continuum level, respectively. *Panel d*: pseudo-spectrum of a source (ID: 06872) with the [O III] λ5007 line truncated on the blue side of the survey spectral range. The pseudo-spectra in *panels e* and *f* – ID: 02250 and 03120 – correspond to the [O III] λ4959,5007 sources unseen in ancillary data and only detected by visual examination of the pseudo-spectra (see Sect. 5.3 for details).